Dynamic Crack Modeling and Analytical Stress Field Analysis in Single-Crystal Silicon Using Quantitative Fractography

Anthony Moulins, Lingyue Ma, Roberto Dugnani, Ricardo J Zednik

PII: S0167-8442(20)30269-X
DOI: https://doi.org/10.1016/j.tafmec.2020.102693
Reference: TAFMEC 102693

To appear in: *Theoretical and Applied Fracture Mechanics*

Received Date: 9 April 2020
Revised Date: 2 July 2020
Accepted Date: 3 July 2020

Please cite this article as: A. Moulins, L. Ma, R. Dugnani, R.J. Zednik, Dynamic Crack Modeling and Analytical Stress Field Analysis in Single-Crystal Silicon Using Quantitative Fractography, *Theoretical and Applied Fracture Mechanics* (2020), doi: https://doi.org/10.1016/j.tafmec.2020.102693

Dynamic Crack Modeling and Analytical Stress Field Analysis in Single-Crystal Silicon Using Quantitative Fractography

Anthony Moulins[1], Lingyue Ma[2], Roberto Dugnani[2,a] and Ricardo J Zednik[1,b]

[1]École de Technologie Supérieure, Université du Québec, Montréal, Canada

[2]UM-Shanghai Jiao Tong University – Joint Institute, Shanghai, China

ABSTRACT

Single-crystal silicon is the fundamental building block enabling today's plethora of integrated electronic components. However, complex mechanical stresses, originating from either direct mechanical loading or thermal cycling, can result in fracture of the constituent silicon, one of the leading causes of semiconductor device failure. Although phenomenological relationships to estimate the fracture strength in silicon have been proposed in the past, no quantitative fractographic method addressing the intrinsic anisotropy of crystals exists. In this work, a fractographic approach using optical confocal microscopy and atomic force microscopy is developed to identify and analyze the cleavage planes associated with dynamic instabilities in single-crystal silicon. We analytically determined the dynamic crack propagation behavior and asymptotic stress field at the crack-tip for unstable, anisotropic, circular cracks in silicon. The fractographic features predicted by the analytical model are consistent with experimental observations, and correctly predict how the {111} planes define the fractographic mirror region (including mirror constant), as well as the {112} planes associated with fractographic Wallner lines. These findings have important consequences in reducing mechanical and thermomechanical failure in semiconductor devices, where the mechanical strength is highly dependent on crystallographic anisotropy.

Keywords: single-crystal silicon, mechanical stress, semiconductor failure, fracture, fractography, anisotropy, dynamic instability, hackle constant, mirror constant.

[a] Corresponding author: roberto.dugnani@sjtu.edu.cn

[b] Corresponding author: ricardo.zednik@etsmtl.ca

I. INTRODUCTION

Single-crystal silicon has been used in semiconductor devices for over half a century. Modern devices in telecommunications, aerospace, and medicine extensively utilize interconnecting silicon-based transistors, capacitors, and sensors[1,2]. Silicon crystals are manufactured into strongly oriented wafers[3,4], resulting in mechanical anisotropy. The presence of preferential cleavage planes is responsible for the specific patterns featured on the fracture surfaces[5–9]. Silicon ingots are usually cut, thinned and used without encapsulation to reduce parasitics, packaged into confined devices for wearability and cost reduction. Unfortunately, as the silicon wafer's thickness is reduced, the effects of steep thermal gradients, expansion coefficient mismatches, and applied external loads become more and more detrimental[10]. The increasingly important nanometer length-scale of modern devices provides additional challenges, although powerful tools to deal with the assessment of silicon can be used as long as there is no breakdown of continuum theory.[11–13] The failure analysis of fractured silicon crystals is essential to understand failure modes and improve semiconductor device reliability. Regretfully, although various relationships to estimate the fracture strength in silicon have been proposed in the past, no industry standard or quantitative fractographic method addressing the intrinsic anisotropy inherent in silicon crystals exists.

Silicon fracture's fractographic signature for (110) fractures was accurately documented and described by the work of Tsai and Mecholsky[14]. Notably, Tsai and Mecholsky attempted to model the crack propagation behavior in silicon to establish the location of the 'mirror-mist boundary.' Although the model could accurately describe the fractographic features observed in (110) fractures, it neglected inertia effects[15] and over-simplistically assumed that all fractographic features formed at the same critical value of the energy release rate. As the mirror region in silicon is bounded by different fracture planes, establishing the boundary of the mirror zone would require separating the critical fracture energy for each set of planes. Tsai and Mecholsky's accurate description of the mirror-mist boundary seemed to be mostly coincidental as cleavage energies in silicon are nearly identical[16]. The weakest cleavage planes in silicon are known to be the {111} planes where $K_{Ic\{111\}}$ = 0.82 MPa√m [17]. However, fracture toughness on the {110} and {100} planes have been reported marginally higher, i.e., $K_{Ic\{110\}}$ = 0.90 MPa√m and $K_{Ic\{100\}}$ = 0.95 MPa√m respectively.

Building upon Tsai and Mecholsky's findings, the work of Dugnani and Verghese[18] recognized that two separate families of branching planes bounded the mirror region. Dugnani and Verghese[18] proposed two alternative methods to measure the mirror radius at 90° (r_{90}) and 45° (r_{45}) with respect to the free surface to account for the two families of branching planes[18]. Dugnani and Verghese phenomenological study explained how to estimate the fracture strength for both families of fracture features but was unable to clarify the origin and relevance of each set of features.

In addition to silicon in the diamond-cubic crystal structure, the literature is rich with fracture surface analysis of a range of anisotropic materials, including lithium fluoride, spinel, sapphire, and other crystal symmetries.[6,8,15,18,19]. Fractographic features, including the relatively flat "mirror" region, the "mist" region[20], "hackles", and Wallner lines[21] are found when the crack-front propagates and possibly interacts with reflected stress waves in single crystals[15,18,19]. Like the work done on single-crystal silicon, these other studies also relied on the phenomenological description of the fracture surface to estimate the material's fracture strength without formally accounting for the inherent anisotropy of the material.

For example, in brittle, isotropic solids, such as small grain ceramics or amorphous materials, the length between the fracture origin and the mirror-mist boundary is commonly correlated to the strength of the material expressed by an empirical equation postulated by Orr[22]:

$$\sigma_f \sqrt{R_m} = A_m \qquad (1)$$

where σ_f is the strength at failure, R_m is the mirror radius; A_m is the empirically obtained material-dependent mirror constant. In small grain ceramics or glasses, the fracture surface is not flat but rather the roughness increases[23,24] as the crack-tip becomes "dynamically unstable". For single crystals, the crack surface is often atomically flat near the fracture origin and eventually, once a critical value of the crack-tip velocity is reached, the crack branches out of the flat mirror plane. The distance between the crack origin and the onset of branching for a given fractographic direction constitutes a recurrent characteristic length associated with dynamic instabilities[15,18], analogous to the mirror radius R_m. Although the

exact process of feature formation is strongly affected by the crystal orientation relative to the stress field, the crystallographic planes associated with specific crystal/stress orientations have not been formally addressed prior to this work[14,15,18,25,26].

The aim of this work is, therefore, to develop a quantitative fractographic methodology to understand the fracture behavior of single-crystal silicon wafers. This is achieved by leveraging 3D surface profilometries of fractured specimens to provide a *"surface angle mapping"* with respect to the main orientation of the crystal. An analytical solution describing the unstable motion of an anisotropic circular crack is developed to help resolve the issue of determining which family of planes is associated with initial crack branching. The relevant *"crystal hackle radius"*, $R_{XH\{110\},}$ which depends on the crystal plane orientations of silicon wafers, is clearly defined and computed at branching for the loading scenario considered. The reciprocal crack lengths at branching are estimated experimentally and correlated with the strength to define the mirror constant or "*crystal hackle constant"*, $A_{XH\{110\}}$. The following section intends to support the claim made in this work that –due to dynamic instabilities– the crack-tip initially deflects from the (110) mirror plane to {111} planes. Furthermore, it will be shown that the features corresponding to the {112} planes were associated with Wallner lines and hence should not be considered as a relevant feature when determining the mechanical strength of a silicon-based device.

II. METHODOLOGY

A. Mirror-Branching Formation

Recently, Dugnani and Ma[27] extended Freund's analytical solution[28] describing the motion of unstable straight-cracks in homogeneous, isotropic, brittle materials, to circular-cracks. This solution was combined with the description of dynamic fields for brittle, anisotropic materials[29] to analyze the stress field at the tip of a crack parallel to the (110) plane. The predicted stress-field was used to estimate the crack-lengths at branching and correlate them to fractographic features. The assumptions made in the model were:

(a) the fracture surface was 'atomically flat' up until crack-branching,

(b) the crack's shape remained nearly circular during the initial propagation.

As shown in Dugnani and Ma's work, the crack radius, a, for flat circular-cracks could be related to the instantaneous crack-tip's velocity through the equation:

$$\frac{a_0}{a} = \left[1 - \left(\frac{\pi}{Y^2}\right)\frac{g(V)-1}{g(V)}\right]^{-1} \quad (2)$$

The term a_0 refers to the initial crack-radius and Y to the local shape factor. For isotropic material and a Poisson's ratio $2/7 < \nu < 1/2$, an approximation for $g(V)$ is given by[28]:

$$g(V) \approx 1 - \chi \text{ with } \chi \equiv V/c_R \quad (3)$$

In the context of crystal fracture, the term c_R was taken as the Rayleigh velocity in the crack propagation direction. For the fracture surfaces considered in this work, crack-growth initially occurred on the (110) plane and eventually branched onto the (111) plane. In the next sections, a brief description of the dynamic crack-field at the crack-tip and how the knowledge of the field was used to predict the crack-branching is given.

B. Dynamic Stress Field in Single-Crystal Silicon

The dynamic stress-field at the crack-tip as a function of the crack propagation direction, β, was computed exactly using Gao et al.'s two-dimensional, dynamic crack propagation model for anisotropic continuous materials based on linear elastic fracture mechanics (LEFM)[29]. The material properties in the direction of the propagating crack were obtained by considering the local compliance matrix in an orthogonal coordinate system defined by the axis of the crack and the β-direction. Similarly, the Rayleigh speed, $c_R(\beta)$, was computed in the direction of the crack propagation. The silicon crystal compliance matrix was evaluated based on values reported in Cho[30]. Based on Gao et al., the dynamic stress-field in the local polar coordinates at β-direction (Figure 1b) was given by:

$$\sigma_{rr} = \frac{K_I}{\sqrt{2\pi r}} Re\left[\frac{f_x(m_1)}{\sqrt{\cos\phi + m_1 \sin\phi}}\frac{D_7}{D_1D_7 - D_3D_5} - \frac{f_x(m_2)}{\sqrt{\cos\phi + m_2 \sin\phi}}\frac{D_5}{D_1D_7 - D_3D_5}\right] \quad (4.a)$$

$$\sigma_{zz} = \frac{K_I}{\sqrt{2\pi r}} Re\left[\frac{f_y(m_1)}{\sqrt{\cos\phi + m_1 \sin\phi}}\frac{D_7}{D_1D_7 - D_3D_5} - \frac{f_y(m_2)}{\sqrt{\cos\phi + m_2 \sin\phi}}\frac{D_5}{D_1D_7 - D_3D_5}\right] \quad (4.b)$$

$$\sigma_{rz} = \frac{K_I}{\sqrt{2\pi r}} Re\left[\frac{f_{xy}(m_1)}{\sqrt{\cos\phi + m_1 \sin\phi}}\frac{D_7}{D_1D_7 - D_3D_5} - \frac{f_{xy}(m_2)}{\sqrt{\cos\phi + m_2 \sin\phi}}\frac{D_5}{D_1D_7 - D_3D_5}\right] \quad (4.c)$$

As explained in Gao et al.[29], m_1 and m_2 are the roots of the characteristic equation (i.e., the strain compatibility equation), ϕ is the angle between the crack-tip and the branching plane considered, and D_i are constants related to both the material properties along the crack propagation direction and the roots of the characteristic equation. The angle ϕ defined as the relative angle between the plane containing the crack before branching, i.e. (110) and the branching-plane (see, Figure 1a). For a semi-circular crack, the angle between the crack-front expanding in the direction β and the (111) plane was computed as:

$$\tan\phi = \sin\beta \cdot \tan(35.2°) \tag{5}$$

Equation (4) and Eq. (5) were used to compute the stresses normal to the (111) plane, $\sigma_{\perp\{111\}}$, as a function of the crack velocity, V. The stress $\sigma_{\perp\{111\}}$ was obtained by first rotating the local, principal stresses at the crack-tip (i.e., σ_{rr} , $\sigma_{\theta\theta}$, σ_{zz}) by an angle β about the *z-axis* (i.e., the $[\bar{1}10]$-axis), as shown in Figure 1b, and subsequently by rotating the stress tensor by 35.2° about the [110]-axis. The expression for $\sigma_{\perp\{111\}}$ was then obtained:

$$\sigma_{\perp\{111\}} = \sin^2(35.2°)\,[\sigma_{rr}\sin^2\beta + \sigma_{\theta\theta}\cos^2\beta] + \sigma_{zz}\cos^2(35.2°)$$
$$-2\sigma_{rz}[\cos(35.2°)\sin(35.2°)\sin\beta] \tag{6}$$

The hoop-stress, $\sigma_{\theta\theta}$, in Eq. (6) was obtained assuming plane-strain conditions at the crack-tip. The value of the velocity, V, corresponding to the crack-branching onto the (111) plane was estimated based on the crack-branching criterion outlined in the next section. Once the branching crack-tip's velocity, V_B, had been established, the crystal hackle radius, R_{XH}, as a function of the crack direction, β, was estimated through Eq. (2).

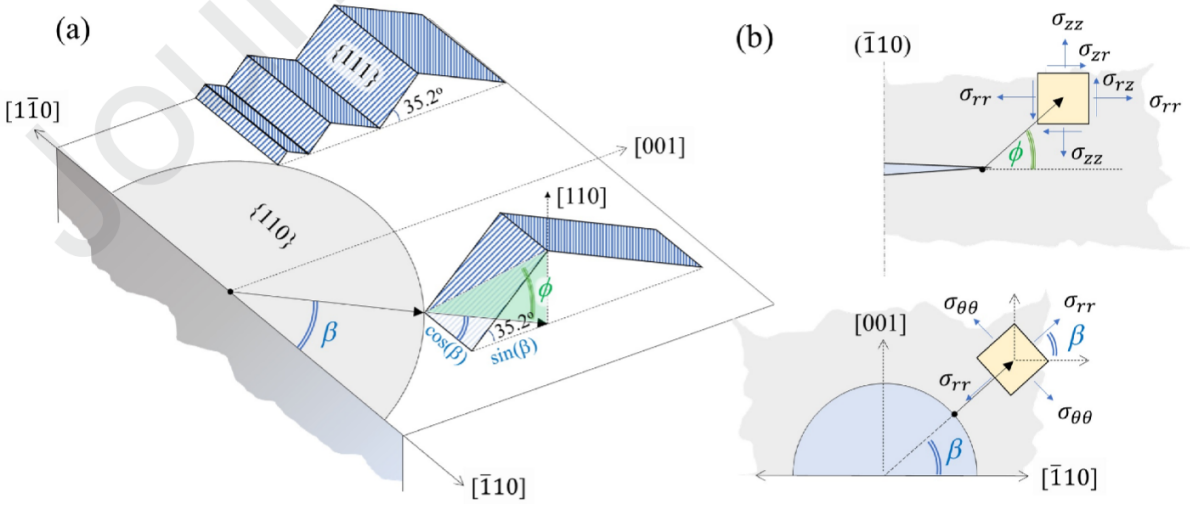

Figure 1: (a) Schematic geometry of crack branching from the (110) to the (111) plane, and (b) the stress field at the crack-tip.

These dynamic stress field calculations are based on the underlying assumption of a continuous material. When the crack is very close in size to the fracture process zone, the continuous material assumption is no longer valid and the continuity assumption in linear elastic fracture mechanics (LEFM) breaks down due to the atomistic nature of matter. In particular, this length scale has been estimated to be about 2-3nm, on the order of about 10 atoms.[31] Nevertheless, the driving force for crack propagation is the total free energy in the entire mechanically strained body. Atomistic modeling of dynamic fractures using large-scale molecular dynamics simulations (MD) have shown that continuum mechanics accounts for virtually the entirety of this strain energy; therefore, although strictly speaking the continuity assumption does not apply at the crack tip, continuum mechanics methods have been shown to provide an excellent description of the dynamic behavior of fast propagating brittle cracks.[32]

C. Crack-Branching Criterion

In order to predict the fractographic features' formation on the fracture surface, the crack branching-criterion had to be first established. In the past, various criteria have been suggested, but no consensus existed on which best described branching in single crystals[33]. In this paper, the maximum K_I criterion was adopted. This criterion assumes that the crack propagates on the (110) plane as long as the normalized stress at the crack-tip orthogonal to the plane, i.e. $\sigma_{(\perp\{110\})} / K_{Ic\{110\}}$, was larger than the normalized stress orthogonal to the {111}-plane, i.e. $\sigma_{(\perp\{111\})} / K_{Ic\{111\}}$:

$$\frac{\sigma_{\perp\{110\}}(\phi,V)}{K_{Ic}\{110\}} > \frac{\sigma_{\perp\{111\}}(\phi,V)}{K_{Ic}\{111\}} \tag{7}$$

K_{Ic} on the (111) plane was chosen based on the value reported by Chen and Leipold[17]. For K_{Ic} on the (110) plane, the mean value was also based on the value reported by Chen and Leipold, but its magnitude adjusted to account for the anisotropy of the fracture toughness as modeled in Cook[34]. Various studies had reported that K_{Ic} was highly anisotropic on the (110) plane, yet relatively uniform on the (111) plane. For instance, Perez[35] indicated that the

fracture toughness on the (110) plane along the [110] direction was lower than along the [100] direction.

D. Uniaxial Flexural Tests

The fracture strength of 41 single-crystal silicon samples cleaved along the (110) plane was obtained and the corresponding fractographic features recorded. Engineered (001) silicon wafers (boron doped) were used (resistivity below 0.001 Ω.m) to work with short, single-crystal beams avoiding high shear stress and defect mobility. The silicon wafers tested in this work had a thickness of H = 0.4 ± 0.1 mm with one side mirror polished. The test specimens had width W = 6±1 mm by length L = 67±15 mm beams, with the [110] direction oriented along the length of the beam. The flexural overloading was performed as three-point bending tests (3PBT) on the tensile side (polished side), and followed ASTM standard

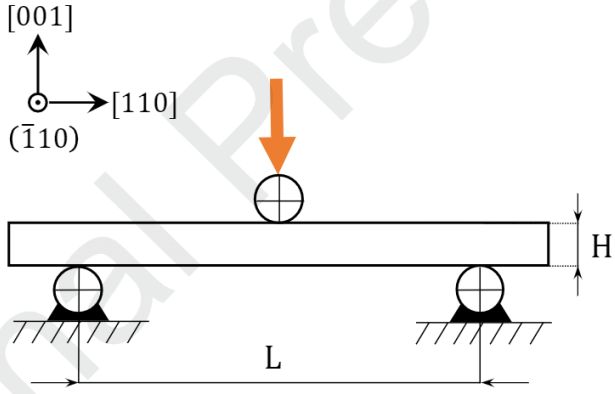

C1161[36]. The 3PBT were conducted on an MTS Model 45 with a 100N load cell (resolution 0.01 N) and roller diameter 5 mm, as illustrated in the schematic below.

Figure 2: Schematic showing a silicon beam undergoing 3PBT.

Test specimens were loaded with a stress rate ranging from 2.5-25MPa/s. No notch or pre-crack was introduced to avoid strong misalignment with the (110) cleavage planes. Linear response and small deflections justified the use of linear elastic beam theory to calculate the fracture strength[36].

E. 3D Surface Characterization

In this section, the technique developed to produce a consistent fractographic characterization of the fracture surfaces and the objective measurements of crystal hackle radii are introduced. Fracture surface maps were obtained using an industrial Olympus Lext OLS4100 confocal microscope with a non-polarized 405 nm laser source of ultraviolet and bright field illumination with 10 nm height resolution and 120 nm lateral resolution to locate fractographic features of interest. A Veeco Enviroscope atomic force microscope (AFM) with tapping mode was used to track the height variation of the crack branching regions with a resolution up to 7.6 x 10^{-2} nm in height and 1.4 nm in the lateral direction.

The following procedure was employed to characterize the 41 silicon fracture surfaces considered:

(1) After the fracture surfaces had been cleaned, 3D surface profilometry near the fracture origin was acquired. The fracture surface was oriented with the free surface parallel to $\langle \bar{1}10 \rangle$, the axis of tension. The image of the fracture surface near the origin was leveled by fitting a plane through 3 reference points within the mirror region and then rotated to align with [110].

(2) The local plane orientation was computed at each pixel using two neighboring data points along [001] and $[1\bar{1}0]$ (see Figure 3). Two vectors were then defined, $\overrightarrow{X_{[1\bar{1}0]}} = \begin{pmatrix} rs \\ 0 \\ \Delta z_{AB} \end{pmatrix}$ and $\overrightarrow{Y_{[001]}} = \begin{pmatrix} 0 \\ rs \\ \Delta z_{AC} \end{pmatrix}$ with rs being the lateral resolution (i.e. unit pixel size), $\Delta z_{AB} = z_B - z_A$, and $\Delta z_{AC} = z_C - z_A$. The angle δ between $\overrightarrow{n_{[110]}}$, the normal vector to (110) and the resulting normal vector $\overrightarrow{n_{[hkl]}}$ (i.e. cross product between $\overrightarrow{X_{[1\bar{1}0]}}$ and $\overrightarrow{Y_{[001]}}$) was obtained locally considering all possible crystallographic orientations. The angle δ was then calculated with respect to the first (110) plane cleaving:

$$\delta = arccos\left\{ -\frac{1}{\sqrt{2}} \frac{\Delta z_{AB} + \Delta z_{AC}}{\sqrt{rs^2 + \Delta z_{AB}{}^2 + \Delta z_{AC}{}^2}} \right\} \quad (8)$$

where $\overrightarrow{n_{[110]}} = \begin{pmatrix} rs \\ rs \\ 0 \end{pmatrix}$ and $\overrightarrow{n_{[hkl]}} = \begin{pmatrix} -\Delta z_{AB} \\ -\Delta z_{AC} \\ rs \end{pmatrix}$.

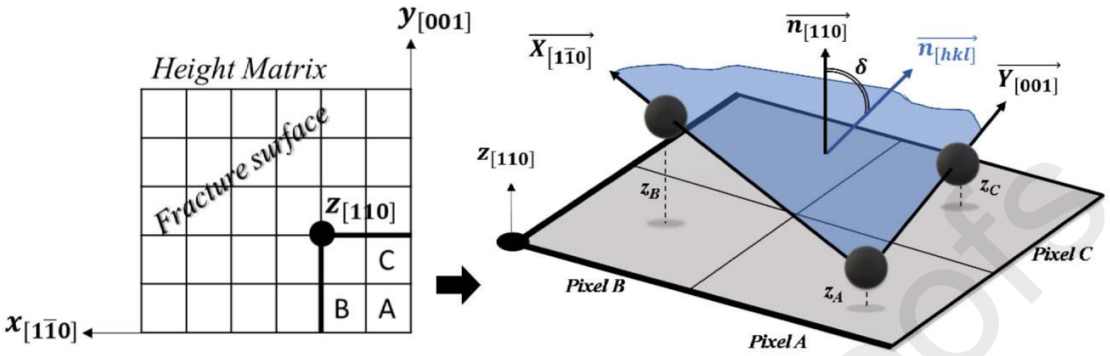

Figure 3: Schematic of height matrix (left) showing the blue crystal facet (right) defined by three adjacent reference points. The angle δ between $\overrightarrow{n_{[hkl]}}$ and $\overrightarrow{n_{[110]}}$ is also shown.

The angle maps thus obtained were used to identify different families of crystallographic planes.

(3) The full map was filtered to highlight the features bounding the mirror region, i.e. the {111} crystallographic facets as shown later. The crack origin was subsequently estimated at the free surface (Fig. 4 a).

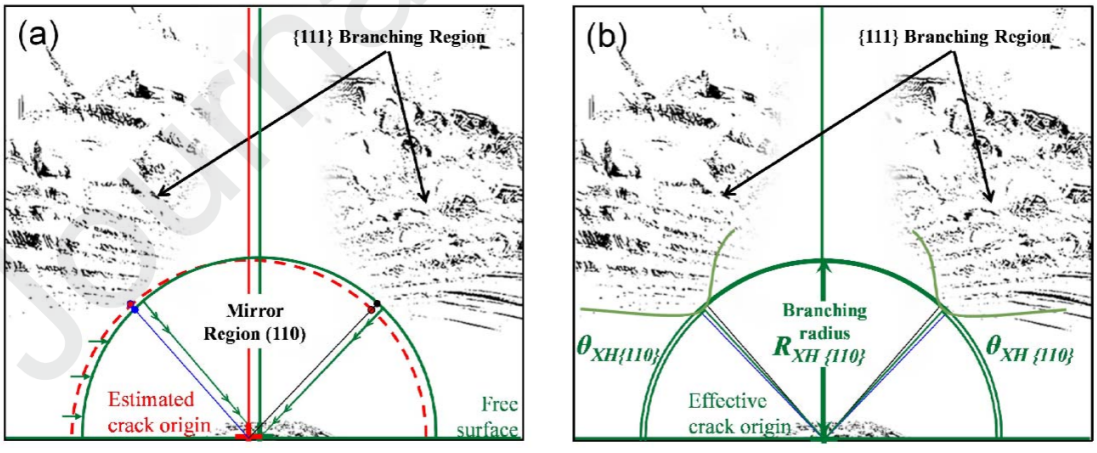

Figure 4: Schematic of a surface angle map using a band-pass filter showing (a) the estimated crack origin and the estimated radii at branching, and (b) the effective crack origin and the computed crystal hackle radius with the branching radius direction with the free surface.

(4) The estimation of the radii at branching was achieved using the function "find" from MATLAB R2019a[37]. The function detected the non-zero elements of the matrix and returned a vector of point indices that had been found. The detected cluster of points (i.e. the branching features) was used to establish the shortest length on each side (i.e. left and right), and their respective orientations, as shown in Fig. 4. (a). The average of these lengths defined the crystal hackle radius $R_{XH\{110\}}$ and crystal hackle radius direction at branching (i.e. branching radius direction) $\theta_{XH\{110\}}$. For specimens that broke 'at the edge', $R_{XH\{110\}}$ and $\theta_{XH\{110\}}$ were obtained considering the single side available.

(5) The effective crack origin locus was defined using an arc of radius $R_{XH\{110\}}$ tangent to the hackle boundary region on both sides with the center along the free surface as shown in Fig. 4 (b). The analytical shape of the {111} mirror to branching boundary was fitted on the filtered surface angle map using the experimental achievements such as $R_{XH\{110\}}$ and $\theta_{XH\{110\}}$ respectively as shown in Fig. 4 (b). The shortest radius $R_{XH\{110\}}$ was subsequently correlated with the strength of the specimens and the orientations of the two sides with respect to the free surface were analyzed in detail.

III. RESULTS

A. Fractography of Single-Crystal Silicon

In this section, the mirror and branching regions are precisely described by AFM profilometries and 3D laser confocal scans. The planes bounding the mirror zone have been separated to objectively provide a measure of crystal hackle radii. AFM surface profilometries were used to generate fractographic surface angle maps Fig. 5 (b) from AFM heights Fig. 5 (a). The strong surface markings in Figure 5 (b) indicated that the crack-tip branched from the (110) plane with facets orientated mostly around ±35° with respect to the mirror plane (i.e. (110) plane at 0°).

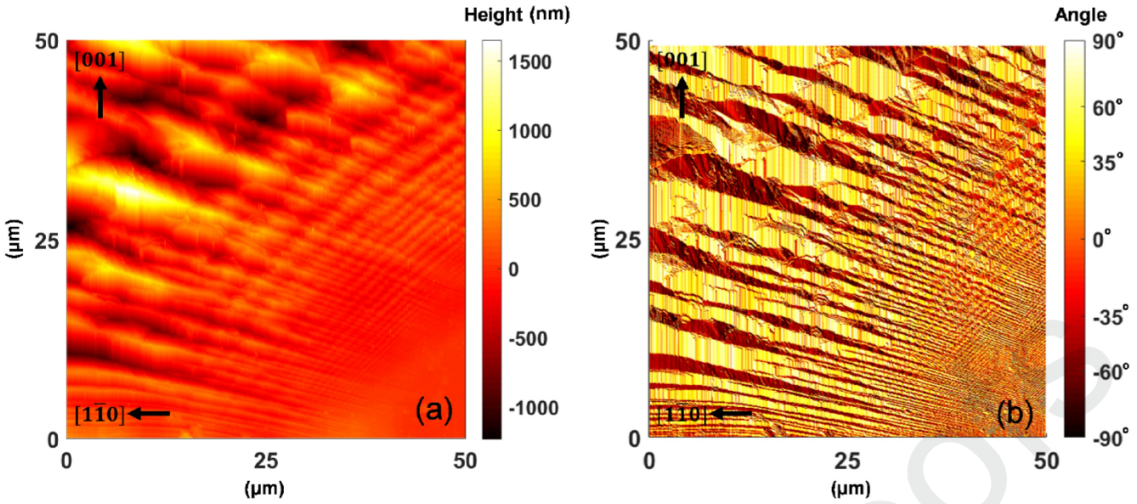

Figure 5: (a) AFM height surface of a silicon sample fractured at 249MPa, and (b) corresponding surface angle map showing the orientations of the crystalline facets at branching.

These pronounced features were associated with the {111} family of planes (theoretically inclined at 35.2°). Additional, less perceivable surface perturbations are also visible in Figure 5 (b) running nearly perpendicular to the principal features. The directionality and inclination of these less obvious marks suggested that they might be related to the {112} family of planes.

Figure 6 shows experimental profilometry carried out by AFM in regions where (a) branching occurred, and (b) at the "cusp". An average planar orientation of 34º with a standard deviation of 11º has been found in concave regions of the profile (a) with an average periodicity of 484 nm. Surface profilometry in Fig. 6(b) indicated an average angle of 20±6 computed from peaks of nearly the same magnitude which are most probably associated with the {112} family of planes. An average height undulation of 183 nm with an average periodicity of 490 nm was found in concave regions of the profile.

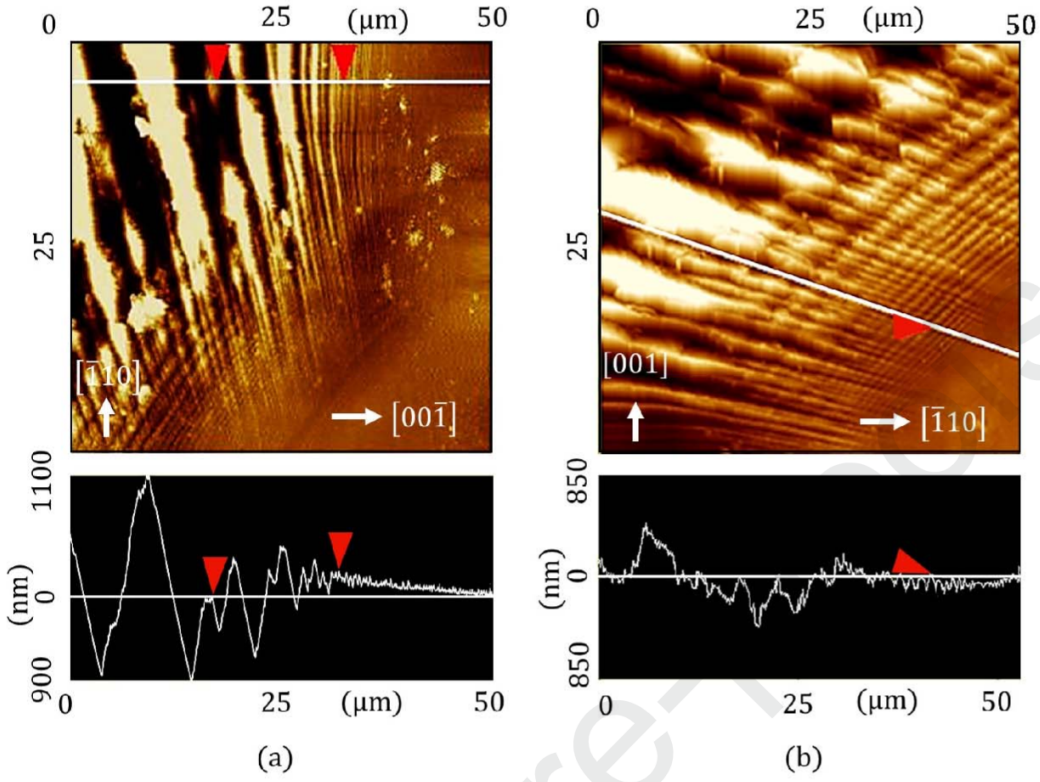

Figure 6: Surface profilometry of the silicon fracture surface with AFM tapping mode tracking crack-tip behavior (a) at branching, and (b) in the "cusp" region.

For most of the fracture surfaces, the mirror appearance was flat with crack traces fanning out of the origin and out of the mirror plane (i.e. the (110) plane) systematically surrounding the mirror region, for instance in Fig. 7. Most of the specimen broke with crack origins 'away from the edge'. Figure 7 shows examples of variations in the fracture morphologies for two samples displaying nearly the same strength. The sample in Figure 7 (a) broke at 204 MPa and the specimen in Figure 7 (b) broke at 212 MPa with a larger flat mirror region. The shapes of the 'flanks' were very similar for both specimens whereas the instability marks above the crack origin (i.e. the so-called "cusp") are significantly less noticeable in Figure 7 (b).

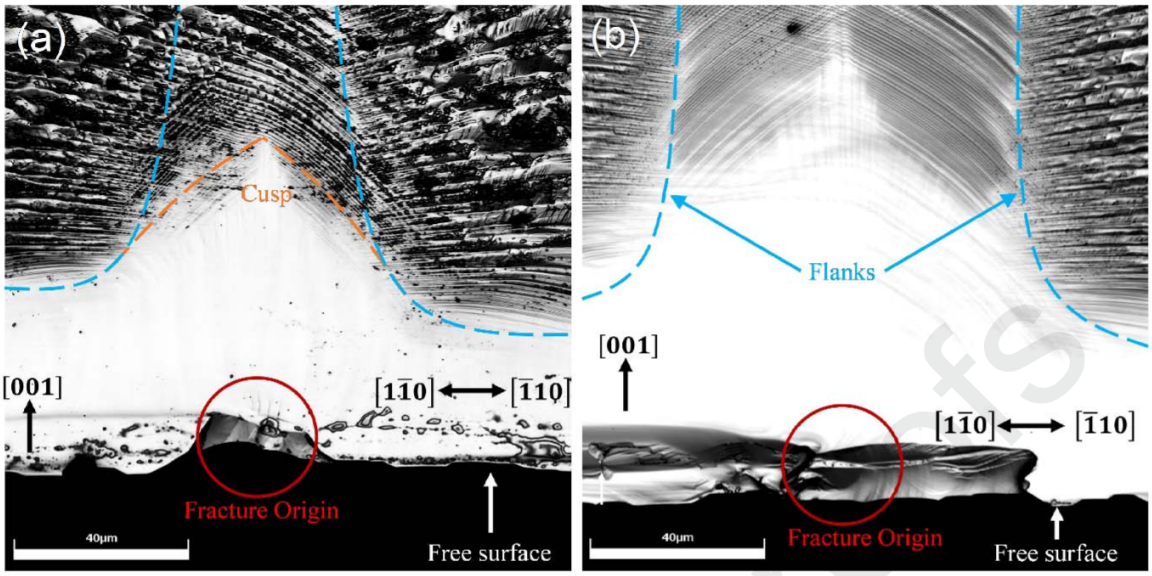

Figure 7: Typical cleaved surfaces of single-crystal silicon under UV laser illumination near the fracture origin.

As outlined previously, 3D confocal optical microscopy was mainly used to characterize the overall region surrounding the mirror region and to generate angular maps of the fracture features. A bandpass filter was applied to retain fractographic features within the *35±10°* band, which were associated with the {111} family of planes. The edge of these features was detected using the methodology outlined in previous sections and compared to the predicted shape from the analytical solution as shown in Figure 8.

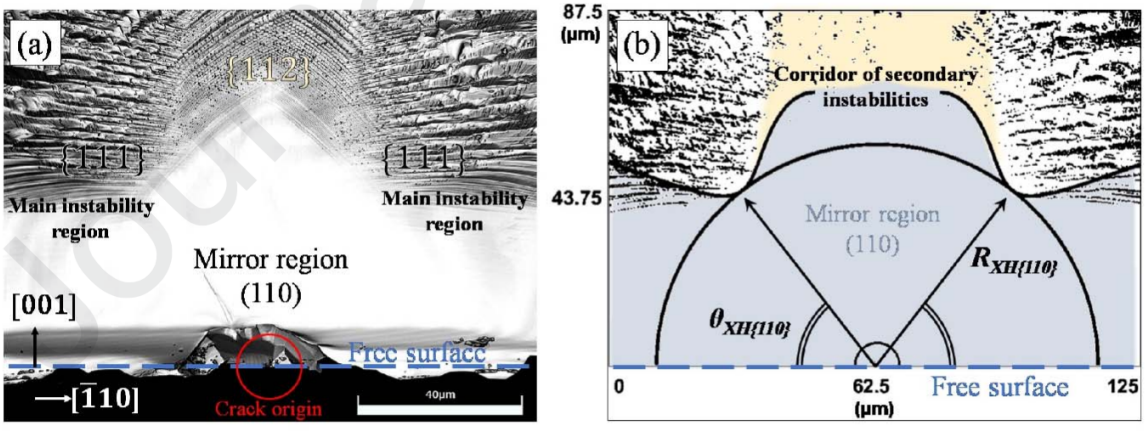

Figure 8: Micrograph of single-crystal silicon fractured at 200MPa (a), and (b)the associated branching region using a surface angle map within a 35±10° band with the predicted shape of the mirror region fitted analytically.

Figure 8 (a) shows an instance of a specimen which broke away from the edge (at 200MPa) and highlights the features formed by different families of planes. Figure 8 (b) shows an example of how the crystal hackle radius was detected from the sample ($R_{XH\{110\}}$ =51.9μm) and the orientation of the crack-tip at branching ($\theta_{XH\{110\}}$ =52.1°) with respect to the free surface. The predicted shape of the mirror region was obtained by fitting the analytical solution with $\theta_{XH\{110\}}$.

Figure 9 (a) shows a summary of the normalized strength vs. the inverse square root of the crystal hackle radii, defined as the shortest distance between the fracture origin and fractographic features corresponding to the {111} plane. Normalizing the crystal hackle radius with the sample's thickness allowed comparing experimental data from the present work with measurements obtained by other authors available in the literature[15,18]. The mirror-radii reported by Tsai and Mecholsky has been included by taking the average of the radii measured at 40° and 50° to be consistent with the data reported by Dugnani and Verghese.

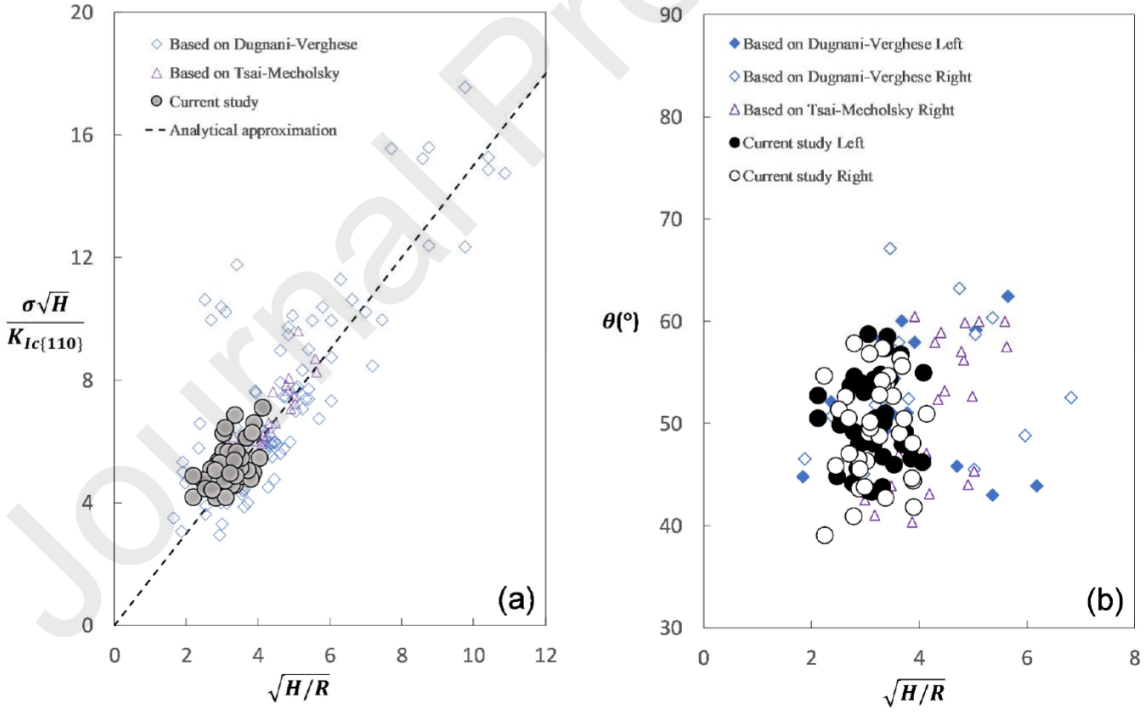

Figure 9: Normalized silicon fracture strengths vs. inverse square root of the crystal hackle radii at branching, including the expected analytical trend (a); branching radii normalized by the thickness vs. crystal-hackle radius orientation with the free surface $\langle\bar{1}10\rangle$ *(b).*

The linear regression of 41 fractured specimens allowed the determination of $A_{XH\{110\}}$=1.47 ±0.24 MPa√m as a scaling parameter for the experimental fracture strengths with an average estimation error of 12% between the experimental strengths and the strengths provided by the analytical regression. The trend obtained in this work was in good agreement with both the experimental data reported by Tsai-Mecholsky (A_m=1.40 MPa√m) and Dugnani and Verghese (A_m=1.39 MPa√m).

Figure 9 (b) shows the comparisons of the crystal hackle radii angles measured with respect to the free surface for the left and right sides. As expected, there were no obvious differences concerning the detection for each side of the branching confirming that the specimens were correctly oriented with [110] and that the fracture symmetry was preserved. In the current study, the averaged orientation θ_{XH} =*50.3*° was located within 43°<θ_{XH}<57°.Angles based on Dugnani and Verghese's work were estimated optically on the left and right side of the origin as well (Fig. 9 b). The asymmetry of the onset of branching from Dugnani and Verghese was more significant than found in this work since the average orientation was more dispersed, such as 43°< $\theta_{average}$ = 53°<67°. The measurements presented in Tsai and Mecholsky were reported for the right side only (Fig. 9 b). In contrast with Dugnani and Verghese, results from Tsai and Mecholsky were located between 40°<$\theta_{average}$ = 51°<60° and hence were more consistent with the results from this work.

B. Analytical Model & Wallner Lines

In this work, the analytical formulation describing the crack propagation and the onset of crack-branching was simplified by assuming that the moving crack-front was semi-circular. To confirm the validity of this simplification, the crack sizes in the [110] direction, a, and c in the [001] direction, were estimated, based on Eq. (2) assuming steady-state crack-propagation in a uniform stress field. Using c_R = 4.5km/s and 5.2km/s on the (110) plane in the [110] direction and [100] direction respectively[38] and substituting into Eq. (2), it was concluded that for a semi-circular, flat crack, 0.98 < a/c <1.1 for 0 < V/c_R < 0.85.

Figure 10 (a) shows the computed crack-branching boundary predicted based on the analytical model described in the previous sections and the failure criterion outlined by Eq. (7). In the same figure, it is also shown an instance of fracture surface from a silicon sample tested in flexure. Branching was predicted to occur first at $R_{XH}/a_0 \approx 2.83$, in the direction β =64°. The predicted branching formation corresponded to a value of the crystal hackle constant (or mirror constant), $A_{XH} = K_{Ic(110)}\sqrt{2.83/1.12} \approx 1.35\text{MPa}\sqrt{\text{m}}$. The range of β from fractographic observations ($\beta \approx 50° \pm 10°$) suggests that, in actual fracture surfaces, *a/c* might differ from the value assumed in this work. Figure 10 (a) shows an instance of a fracture surface on the {110}-plane with the corresponding branching radius and Wallner lines patterns based on the analytical solution. Although the fractographic pattern was very similar, the minor discrepancies can be explained by the simplifying assumptions used in the analytical calculations. In particular, one of the known effects of crack branching is a reduction in crack velocity, which was not taken into account by the present analytical model. The breaking down of this assumption can explain why the shape of the mirror boundary and Wallner lines suffered from systematic error when compared to experimental

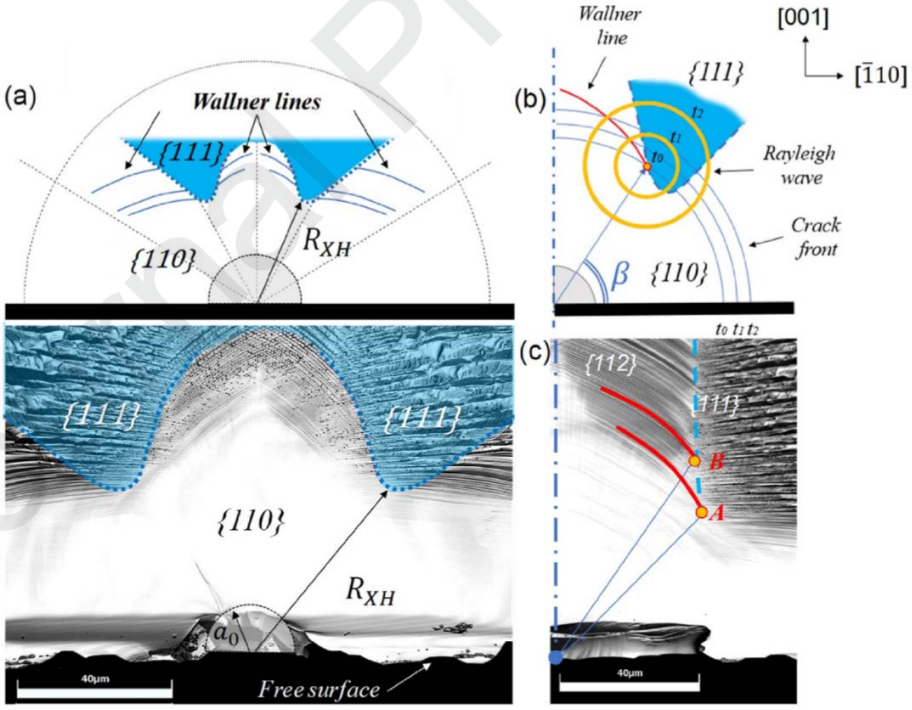

observations; further research into the effect of a change in crack velocity is ongoing.

Figure 10: (a) Analytical crack branching contour from the {110} to the {111} with actual fracture surface with the corresponding R_{XH} and (b) representation of Wallner line

formation and (c) red lines show the predicted location of the Wallner lines starting at crack-branching points A and B on a tested sample's fracture surface (lower right).

As the crack locally branched from the (110) to the {111} planes, acoustic waves were triggered at branching points. These acoustic waves interacted with the crack-front propagating on the (110) plane, with temporary excursion out-of-plane, forming rib-shaped surface markings, i.e. the Wallner lines. In this section, the location of Wallner lines on the (110) plane was estimated based on the geometry and loading considered. For a given crack branching location (e.g. points A and B in Figure 10 (c)), the Wallner line formation was predicted by the intersecting points for the propagating acoustic wave-front and the crack-front on the (110) plane (Figure 10 (b)). For a given crack-direction β, the acoustic wave speed, i.e. Rayleigh speed c_R and the crack speed V were taken based on Sherman's reported values[38] (V/c_R between 0.28 and 0.38 for the branching locations considered). An instance of two Wallner lines, as predicted in this analysis near the symmetry plane, is shown in Figure 10 (c).

IV. DISCUSSION

A. Dynamic Crack-Tip Instabilities

Both sharp hackles or {111} "prism-like" features and features formed by cracks propagating on the {112} planes, were found to bound the mirror-region, in good agreement with the literature[9,16,39,40]. The {111} hackles formed during crack propagation (as illustrated in Fig. 1) have not been used in the past for quantitative fractography, although, as discussed in Sherman and others[39,41–43], they were consistently observed and they might be useful in estimating mechanical and/or physical properties of crystals. We rectify this missed opportunity (as detailed in Fig. 3-4) by leveraging fractographic features to calculate the fracture strength. The use of surface angle maps rather than feature-heights conventionally used, helps to better discriminate between relevant fractographic regions (as illustrated in Fig. 5). This approach is based on the fact that the fracture surface of single crystal silicon comprises features formed on different crystallographic planes (see Fig. 6), and we show that only {111} is induced by dynamic instabilities (as described in Fig. 7-8). We confirm

that the {112} features are 'secondary features', resulting from the interaction between acoustic waves and the crack-front, similar to Wallner lines in amorphous materials. Although it has been shown by Dugnani and Verghese[18] that secondary features at the 'cusp' did correlate with the fracture strength of the sample, secondary markings are likely less reliable as they can be susceptible to unpredictable factors including reflected acoustic waves from sample surfaces and defects. Additionally, we observe that Wallner lines at the 'cusp' are not always present, for example as shown in Fig. 7, hence any method relying on this feature cannot be reliably implemented.

Figure 9 (b) shows a plot of the crystal hackle radius orientation with respect to the free surface $\langle \bar{1}10 \rangle$, $\theta_{XH\{110\}}$ vs. $(H/R)^{1/2}$. No significant angular variations were noted between the left and right sides of the mirror boundaries, which suggests not only that the crack developed symmetrically regardless of the initial flaw shape, but also those dynamic instabilities were triggered at well-defined values of the stress intensity factor. This observation can also be inferred from the symmetric appearance of all fracture surfaces measured, for instance, in Figure 10. In this work, the crystal direction where first crack branching occurred was measured in 41 specimens and estimated at $\theta_{XH\{110\}} = 50.3 \pm 3.58°$. Notably, the observed first branching angle was very consistent in the range $2 < (H/R)^{1/2} < 7$. This observation is important, as the critical fracture strength on the {110} planes was thought to depend on the crack propagation direction, hence significant variations in $\theta_{XH\{110\}}$ would naturally imply that variations in A_{XH} should also be expected. The effect of $(H/R)^{1/2} > 2$ on $\theta_{XH\{110\}}$ could not be directly observed in the sample sizes considered in this work.

B. Crack-Branching Model

We considered the behavior of fast-moving circular cracks in an anisotropic material, single-crystal silicon. The crack-branching criterion used was the maximum-hoop stress. The fracture toughness on the {111} planes was assumed uniform (i.e. $K_{Ic\{111\}} = 0.82$ MPa$\sqrt{m}$), while on the {110} planes, it depended on the crack propagation direction. Assuming $K_{Ic\{110\}} = 0.90$MPa$\sqrt{m}$, the predicted crystal hackle constant corresponding to crack-branching from the (110) to the {111} planes, was estimated as $A_{XH} = 1.35$MPa$\sqrt{m}$. The relative uncertainty

on the experimental $A_{XH\{110\}}$ was calculated following the law of the propagation of variance through the corresponding quadratic sum of each of the relative uncertainties of its associated variables (i.e. the strength and $R_{XH\{110\}}$). The experimental crystal hackle radius was $A_{XH\{110\}}$ = 1.47±0.24 MPa√m and provided nearly the same scaling (i.e. the same crystal hackle constant) as the value computed analytically. The marginally smaller magnitude predicted by the analytical model can be explained in part by the model simplifications, the uncertainties associated with the fracture strength of the material, and by the fact that crack-branching might be occurring at smaller crystal hackle radii than reported by the experiments but undetected due to the small feature size relative to the incident radiation wavelength (UV and visible light). Experimental support to this last explanation was provided by Cramer's description of fractures on the silicon {110}-plane[44]. Cramer reported that, at relatively high crack speeds, {111} features formed on the fracture surface but appeared 'mirror-like' by optical microscopy.

The experimental and analytical crystal mirror and hackle constants obtained in this work are in good agreement with the reported experimental values from Dugnani and Verghese, i.e A_m = 1.54MPa√m. Dugnani and Verghese's higher magnitude for the mirror constant, A_m, can be attributed to the fact that R_m was measured at fixed angles, hence its magnitude was always larger or equal to the values obtained through the methodology described in this work. The values reported by Tsai-Mecholsky seemed to be the most consistent with A_m = 1.39MPa√m (from 24 samples). Tsai-Mecholsky's trend consistency can be explained by the fact that the surface defects were also consistent in size and shape, as they were introduced artificially by indentation. The symmetric and nearly circular sizes of the indented flaws resulted in more consistent initial crack shapes compared to the naturally occurring defects considered in the present work.

The analytical description of the mirror region matched the experimentally observed boundaries obtained with the procedure developed in this study (Fig. 8). The differences between the analytical and experimental shape of the mirror boundary can be attributed mostly to the simplifications in the analytical solution which, for instance, assumes the crack remains circular both before and after branching. The analytical solution can also predict the formation of secondary features, including Wallner lines. The formation of these secondary

features was correctly predicted. However, one of the known effects of crack branching is a reduction in crack velocity, which was not taken into account by the present analytical model and is an avenue for future study. In particular, the "cusp" predicted by the analytical model was in a region where the crack-tip velocity and shape were no longer uniform, and hence beyond the applicability range of the analytical solution. The breaking down of the model's assumptions can explain why the shape of the mirror boundary and Wallner lines in Fig. 10 b) and c) were reliable, yet suffered from systematic error when compared to experimental observations. In addition, our analytical model employs dynamic stress field calculations based on continuum fracture mechanics. At very small length-scales (smaller than 2-3nm), the discrete, atomistic nature of matter limits the applicability of this assumption.[31] Nevertheless, molecular dynamics simulations have shown that continuum mechanics is able to account for the vast majority of the total free strain energy in the body.[32] The release of this strain energy is the driving force for crack propagation, and although the use of continuum mechanics is therefore justified, this may partially explain the minor systematic error observed. The model predictions are nonetheless extremely useful, as they correctly predict the formation of secondary features and help explain why such secondary features cannot be relied upon when estimating the strength of fractured samples.

CONCLUSIONS

In this work, a novel framework for the fractographic analysis of silicon fracture on the (110) plane was introduced. Unlike previous work, this method identifies specific cleavage planes associated with dynamic instabilities, thereby accounting for the intrinsic anisotropy of single-crystal silicon. Both confocal optical microscopy and atomic force microscopy were used to characterize, using 3D surface profilometry, relevant cleavage planes associated with all important fractographic features.

Surface angle maps were computed from 3D surface profilometries, thereby identifying the crystallographic planes when first crack branching occurs. An analytical dynamic fracture model was also developed and used to establish which cleavage plane best correlates with the fracture strength. With the aid of the analytical model, it was determined that features

corresponding to the {112} planes were Wallner lines, and hence they were not relevant when estimating the strength. The shortest length between crack origin and the detected {111} cluster of points at crack branching delineate the mirror-boundary; these radii were subsequently correlated with experimental strengths to extract the experimental crystal hackle constant (mirror constant) $A_{XH\{110\}} = 1.47 \pm 0.24 \text{MPa}\sqrt{\text{m}}$.

The scaling, branching planes, and fractographic patterns predicted by the analytical model are consistent with the experimental findings, and correctly predict that the {111} planes bound the mirror region, whereas the {112} planes are associated with Wallner lines. Furthermore, the analytically computed crystal hackle constant was found to be within 8% of the experimental observation. These important findings improve our understanding of the fracture in single-crystal silicon and help elucidate mechanical and thermomechanical failure modes in semiconductor devices. In particular, the consequence is that the lithographic patterning and manufacture of semiconductor devices should take into account the mechanical anisotropy of crystallographic orientations to improve fracture toughness and thereby prolong service life and enhance reliability.

ACKNOWLEDGMENTS

The authors would like to thank the Natural Sciences and Engineering Research Council of Canada (NSERC) Discovery Grant RGPIN-2015-04185, MITACS Globalink Grant IT09006, and the ÉTS Fonds pour la collaboration international de recherche for funding. The authors also wish to acknowledge Guillaume Grosse and Alexandre Esteves, who contributed by writing the computer code for generating the surface angle mapping.

REFERENCES

1. Blakemore, J. S. Semiconducting and other major properties of GaAs. *J. Appl. Phys.* **53**, R123 (1982).
2. Hjort, K., Soderkvist, J. & Schweitz, J. A. Gallium arsenide as a mechanical material.

J. Micromechanics Microengineering **4**, 1–13 (1994).

3. Lekhnitskii, S. *Theory of elasticity of an anisotropic elastic body*. (Holden-Day, 1963).

4. Hopcroft, M., Nix, W. D. & Kenny, T. W. What is the Young ' s Modulus of Silicon ? *J. Microelectromechanical Syst.* **19**, 229–238 (2010).

5. Ebrahimi, F. & Kalwani, L. Fracture anisotropy in silicon single crystal. *Mater. Sci. Eng. A* **268**, 116–126 (1999).

6. Quinn, G. D. *NIST Recommended Practice Guide: Fractography of Ceramics and Glasses*. *National Institute of Standards and Technology; NIST Recommended* **191**, (NIST SP - 960-16, 2016).

7. Kirchner, H. P. & Kirchner, J. W. Fracture Mechanics of Fracture Mirrors. *J. Am. Ceram. Soc.* **62**, 198–202 (1979).

8. Mecholsky, J., Freiman, S. W. & Rice, R. W. Fractographic Analysis of Ceramics. in *Fractography in Failure Analysis* 363-363–17 (ASTM International, 1978). doi:10.1520/STP38101S

9. Sherman, D. Fractography of Dynamic Crack Propagation in Silicon Crystal. *Key Eng. Mater.* **409**, 55–64 (2009).

10. Uchida, K. *et al.* Experimental study of biaxial and uniaxial strain effects on carrier mobility in bulk and ultrathin-body SOI MOSFETs. in *IEDM Technical Digest. IEEE International Electron Devices Meeting, 2004.* 229–232 doi:10.1109/IEDM.2004.1419116

11. Sumigawa, T. *et al.* Griffith Criterion for Nanoscale Stress Singularity in Brittle Silicon. *ACS Nano* **11**, 6271–6276 (2017).

12. Gallo, P., Yan, Y., Sumigawa, T. & Kitamura, T. Fracture behavior of nanoscale notched silicon beams investigated by the theory of critical distances. *Adv. Theory Simulations* **1**, 1700006 (2020).

13. Gallo, P., Hagiwara, Y., Shimada, T. & Kitamura, T. Strain energy density approach for brittle fracture from nano to macroscale and breakdown of continuum theory. *Theor. Appl. Fract. Mech.* **103**, 102300 (2019).

14. Tsai, Y. L. & Mecholsky, J. Fractal fracture of single crystal silicon. *J. Mater. Res.* **6**, 1248–1263 (1991).

15. Tsai, Y. L. & Mecholsky, J. Fracture mechanics description of fracture mirror formation in single crystals. *Int. J. Fract.* **57**, 167–182 (1992).

16. Sherman, D. Energy considerations in crack deflection phenomenon in single crystal silicon. in *International Journal of Fracture* **140**, 125–140 (2006).

17. Chen, C. P. & Leipold, M. H. Fracture toughness of silicon. (1980).

18. Dugnani, R. & Verghese, P. Failure analysis of modern silicon dice. *Int. J. Appl. Ceram. Technol.* **11**, 783–792 (2014).

19. Sauthoff, K. *et al.* Nonlinear dynamic instability in brittle fracture of GaAs. *Phys. Rev. B* **60**, 4789–4795 (1999).

20. ASTM. Standard practice for fractographic analysis of fracture mirror sizes in ceramics and glasses. *ASTM Int.* 1–15 (2010). doi:10.1520/C1678-10

21. Wallner, H. Linienstrukturen an Bruchflächen. *Zeitschrift für Phys.* **114**, 368–378 (1939).

22. Orr, L. Practical Analysis of Fractures in Glass Windows. *Mater. Res. Stand.* **12**, 21–23 (1972).

23. Dugnani, R. & Zednik, R. J. Flexural strength by fractography in modern brittle materials. *J. Am. Ceram. Soc.* **96**, 3908–3914 (2013).

24. Dugnani, R. & Zednik, R. J. Geometric description of fracture surface features in isotropic brittle solids. *Eng. Fract. Mech.* **165**, 87–97 (2016).

25. Abdel-Latif, A. I. A., Tressler, R. E. & Bradt, R. C. Fracture mirror formation in single crystal alumina. *Appl. Non-metals* 933–939 (1978).

26. Mecholsky, J. J., Freiman, S. W. & Rice, R. W. Fracture surface analysis of ceramics. *J. Mater. Sci.* **11**, 1310–1319 (1976).

27. Dugnani, R. & Ma, L. Energy release rate of moving circular-cracks. *Eng. Fract. Mech.* **213**, 118–130 (2019).

28. Freund, L. B. Crack propagation in an elastic solid subjected to general loading—I. Constant rate of extension. *J. Mech. Phys. Solids* **20**, 129–140 (1972).

29. Gao, X., Kang, X. W. & Wang, H. G. Dynamic crack tip fields and dynamic crack propagation characteristics of anisotropic material. *Theor. Appl. Fract. Mech.* **51**, 73–85 (2009).

30. Cho, C. H. Characterization of Young's modulus of silicon versus temperature using a "beam deflection" method with a four-point bending fixture. *Curr. Appl. Phys.* **9**, 538–545 (2009).

31. Shimada, T., Ouchi, K., Chihara, Y. & Kitamura, T. Breakdown of continuum fracture mechanics at the nanoscale. *Sci. Rep.* **5**, 1–6 (2015).

32. Buehler, M. J. & Gao, H. Dynamical fracture instabilities due to local hyperelasticity at crack tips. *Nature* **439**, 307–310 (2006).

33. Azhdari, A. & Nemat-Nasser, S. Energy-release rate and crack kinking in anisotropic brittle solids. *J. Mech. Phys. Solids* **44**, 929–951 (1996).

34. Cook, R. F. Strength and sharp contact fracture of silicon. *J. Mater. Sci.* **41**, 841–872 (2006).

35. Pérez, R. & Gumbsch, P. Directional Anisotropy in the Cleavage Fracture of Silicon. *Phys. Rev. Lett.* **84**, 5347–5350 (2000).

36. ASTM. Standard Test Method for Flexural Strength of Advanced Ceramics at Ambient Temperature. *ASTM Int.* 1–19 (2013). doi:10.1520/C1161-13

37. MATLAB version 9.6.0.1174912 (R2019a) Update 5. (2019).

38. Sherman, D. Macroscopic and microscopic examination of the relationship between crack velocity and path and Rayleigh surface wave speed in single crystal silicon. *J. Mech. Phys. Solids* **53**, 2742–2757 (2005).

39. Sherman, D., Markovitz, M. & Barkai, O. Dynamic instabilities in {111} silicon. *J. Mech. Phys. Solids* **56**, 376–387 (2008).

40. Ben-Bashat Bergman, L. & Sherman, D. On dynamic surface instabilities of cracks in brittle crystals. *Int. J. Eng. Sci.* **136**, 78–91 (2019).

41. Sherman, D. & Be'ery, I. From crack deflection to lattice vibrations - Macro to atomistic examination of dynamic cleavage fracture. *J. Mech. Phys. Solids* **52**, 1743–1761 (2004).

42. Kermode, J. R. *et al.* Low-speed fracture instabilities in a brittle crystal. *Nature* **455**, 1224–1227 (2008).

43. Kaufman, M. J. & Forty, A. J. A detailed fractographic analysis of cleavage steps in silicon. *J. Mater. Sci.* **21**, 3167–3172 (1986).

44. Cramer, T., Wanner, A. & Gumbsch, P. Energy Dissipation and Path Instabilities in Dynamic Fracture of Silicon Single Crystals. *Phys. Rev. Lett.* **85**, 788–791 (2000).

Conflict of Interest Statement

The authors declare that there are no conflicts of interest regarding our manuscript "Dynamic Crack Modeling and Analytical Stress Field Analysis in Single-Crystal Silicon Using Quantitative Fractography" submitted on April 9, 2020.

This research was funded using the following grants:

- Natural Sciences and Engineering Research Council of Canada (NSERC) Discovery Grant RGPIN-2015-04185
- MITACS Globalink Grant IT09006
- ÉTS Fonds pour la collaboration international de recherche

Anthony Moulins, Lingyue Ma, Roberto Dugnani, and Ricardo J Zednik

Highlights

- Quantitative fractographic method considers the intrinsic anisotropy of crystals.
- Cleavage planes are associated with fractographic features in monocrystal silicon.
- Analytical model shows how {111} planes are related to the mirror region.
- Analytical model explains how {112} planes are associated with Wallner lines.
- Results allow strength estimation in single crystal silicon by fractography.